Hydrochemical performance and mineralogical evolution of a dispersed alkaline substrate (DAS) remediating the highly polluted acid mine drainage in the full scale passive treatment of Mina Esperanza (SW, Spain)

Running title: Mineralogy and hydrochemistry of the passive treatment in Mina Esperanza

Manuel A. Caraballo[1*], Francisco Macías[1], José Miguel Nieto[1], Julio Castillo[1], Dino Quispe[1] and Carlos Ayora[2].

1 Geology Department, University of Huelva, Campus "El Carmen", E-21071 Huelva, Spain

2 Institute of Environmental Assessment and Water Research, IDÆA – CSIC, Jordi Girona 18, 08034 Barcelona, Spain

---

[*] Corresponding author. Tel.: +34-95-921-9834; fax: +34-95-921-9810

E-mail address: manuel.caraballo@dgeo.uhu.es (Manuel A. Caraballo)

Abstract

Acid mine drainage remediation is an unresolved matter in abandoned mining districts around the world. Development and implementation of passive treatment systems in these areas are commonly focused on engineering and water quality aspects; nevertheless, neoformed mineral phases precipitated within the reactive material of those passive treatments play an essential role on their performance. After 20 months of operation and monitoring, the limestone based passive treatment system implemented in Mina Esperanza (SW Spain) was sampled to study in detail the relationship between water chemistry, mineral composition of the neoformed precipitates and treatment performance. Water chemical profiles showed the existence of three precipitation zones controlled by Fe, Al and Zn hydrochemistry and also the migration with time of those precipitation zones downward the reactive material. This precipitation zones were also confirmed by the mineral study performed to the solid samples, where schwertmannite and goethite, hydrobasaluminite and Zn rich green rust were the mineral phases controlling metal removal in the Fe, Al and Zn precipitation zones, respectively. Fe and Al precipitates were observed to play a critical role in the time evolution of the reactive material hydraulic conductivity. Furthermore, Al precipitates passivated to some extent limestone grains by armoring, although migration of the Fe precipitation zone and Al redissolution activate again the limestone grains. A higher proportion of limestone in the reactive mixture and the addition of new reagents to the bottom section of the reactive material (to enhance the reducing environment and to promote divalent metals removal) are proposed on the basis to this hydrochemical and mineralogical study for a future new design in the Mina Esperanza passive treatment system.

Keywords

Acid mine drainage, passive treatment system, schwertmannite, hydrobasaluminite, green rust

1. Introduction

Acid mine drainage (AMD) is an ancient and widespread environmental problem providing one of the most extreme and unique environments on the Earth. Polluted waters in mining areas typically exhibit low pH and high metal contents as a result of the sulfide dissolution taking place after the exposure of these minerals to the surface oxic conditions (Bigham and Nordstrom, 2000).

The Iberian Pyrite Belt (IPB) in the SW of the Iberian Peninsula is one of the largest massive sulfide provinces in the world with original estimated reserves in the order of 1700 Mt of sulfide ore (Sáez et al., 1999). This region is also known to be a world-class example of AMD pollution where the long term effect of this contamination is dated back prior to roman times (Nocete et al., 2005). The wide exposure of sulfide rich residues and the lack of carbonate rocks in this region not only create a ubiquitous problem of AMD with very high metal content (Sarmiento et al., 2009).

AMD at abandoned mine districts is typically faced by the implementation of passive treatment technologies (Younger et al., 2002). Remediation techniques like permeable reactive barriers, vertical flow wetlands or aerobic wetlands have been successfully employed to improve water quality in coal mining areas affected by AMD (Caraballo et al., 2010; Jarvis et al., 2006; Johnson and Hallberg, 2005). However, the high metal content observed in the AMD from the IPB severely reduces the efficiency of conventional passive treatment systems. To overcome the common clogging problems and losing of reactivity exhibit by traditional reactive substrates submitted to AMD with high metal contents, a novel reactive mixture known as Dispersed Alkaline Substrate (DAS) was successfully tested in both laboratory (Rötting et al., 2008c) and field experiments (Caraballo et al., 2009a; Rötting et al., 2008b). Limestone-DAS is a high porosity-high reactivity substrate made of a mixture of 80 % v/v pine wood shavings and 20 % v/v limestone sand.

Passive treatments studies are commonly focused on water chemistry improvement and metal removal, obviating the important role exerted by mineral precipitates in AMD water chemistry and passive treatments performance. Specifically, iron and aluminum precipitates play a key role buffering water pH (Bigham and Nordstrom, 2000), inducing reactive material passivation (Caraballo et al., 2009b), reducing the hydraulic conductivity of the reactive material (Rötting et al., 2008b) and removing other toxic metals by coprecipitation and/or absorption processes (Caraballo et al., 2009a).

This work will present the hydrochemical and mineralogical information obtained in the limestone-DAS passive treatment in Mina Esperanza after 20 month of operation. This is the first full scale experiment of DAS remediation systems. On the basis of the role played by precipitates in limestone consumption/passivation, hydraulic conductivity evolution and removal efficiency, some improvements to the original design will be discussed.

2. Materials and methods

2.1. Field site and treatment description

The passive treatment system implemented in Mina Esperanza is located in the northern part of the IPB, in South-western Spain (Fig. 1A). As many other AMD discharges at the IPB, the highly polluted water emerging from the adit of Mina Esperanza is characterized by low pH, high electrical conductivity and high metal content. A detailed compositional range of metal concentration and physical-chemical parameters obtained at the adit mouth after monitoring the system for 20 months (March 2007-October 2008) is shown in Table 1.

The AMD emerging from the adit is directed by a concrete opened channel to the reactive tank. Water inflow was controlled to obtain common inflow rates ranging from 43 to 86 m^3/day. The reactive tank has a volume of 480 m^3 (15 m x 8 m x 4m, long x wide x deep) and was filled with a 0.5 m bottom drain layer of inert quartz gravel and an overlaying 2.5 m limestone-DAS layer (Fig. 1B). Water flow through the reactive material was gravity forced from top to bottom, finally emerging from the top of the water collecting well, creating an initial supernatant depth of 0.25 m and a freeboard of 0.75 m (Fig. 1B). The reactive tank was equipped with 9 sampling tubes (1 cm inner diameter) at different depths: -25 cm and -5 cm in the supernatant, 15, 25, 50, 65, 80, 175 and 230 cm within the reactive material. Zero corresponds to the water-reactive interface and sample at 280 cm to the emerging water at the collecting well. Residence time for the AMD within the reactive material typically ranged from 2.5 to 5 days. Finally, the water emerging from the reactive tank is conducted to a 60 m^3 decantation pond by a concrete opened channel.

2.2. Water and solid samplings

For the sake of simplicity, the current study is focused in three water sampling campaigns (August-2007, November-2007 and May-2008), corresponding to 5, 8 and 14 months after the treatment commissioning. Water samples were filtered immediately after collection through 0.1 μm Millipore filters on Millipore syringe filter holders, acidified in the field to pH < 1 with suprapur HNO_3 and stored at 4 ºC in 60 mL sterile polypropylene containers until analyzed. Temperature and electrical conductivity were measured in situ using a portable CM35 meter (Crison®) with 3 point calibration (147 and 1413 μS/cm and 12.88 mS/cm). The pH and redox potential were measured using a PH25 meter (Crison®) with Crison electrodes. Redox potential and pH were controlled and calibrated using 2 points (240–470 mV) and 3 points (pH 4.01–7.00–9.21), respectively, with Crison standard solutions. Redox potential measurements were corrected to the Standard Hydrogen Electrode. Dissolved O_2 was measured with an auto-calibrating Hanna® portable meter and gross alkalinity was determined using CHEMetrics® Total Titrets® (range 10–100 or 100–1000 mg/L as $CaCO_3$ equivalents, accuracy approximately 5%).

After the treatment closure in October 2008, 13 solid samples were collected to characterize the neoformed precipitates within the reactive material profile. Sample depths selected were: 0–5, 5–15, 15–20, 20–35, 35–50, 50–85, 85-110, 110-135, 135-160, 160-185, 185-210, 210-240 and 240–250 cm. Samples were heated at 30 °C until completely dry and were ground in a tungsten carbide mill for 2 min.

Hydraulic conductivity (m/day) was calculated according to Darcy's Law:

$$K = \frac{Q \cdot L}{A \cdot \Delta h} \qquad (1)$$

where Q (m^3/day) is flow rate, A (m^2) is tank cross-section perpendicular to flow, and L and Δh (m) are distance and head-loss between supernatant and outflow, respectively.

2.3. Analytical techniques

Concentrations of dissolved Al, As, Ba, Be, Ca, Cd, Co, Cr, Cu, Fe, K, Li, Mg, Mn, Na, Ni, S, Si, Sr, Ti, V and Zn in water samples were determined by Inductively Coupled Plasma Atomic Emission Spectrometry (ICP-AES Jobin- Ybon Ultima2) using a protocol especially designed for AMD samples (Tyler et al., 2004). Analysis was performed at the Central Research Services of the University of Huelva (CRSUH). Multielement standard solutions prepared from single certified standards supplied by SCP SCIENCE were used for calibration. They were run at the beginning and at the end of each analytical series. Certified Reference Material SRM-1640 NIST fresh-water-type and inter-laboratory standard IRMM-N3 wastewater test material (European

Commission Institute for Reference Materials and Measurements) were also analyzed. Detection limits were calculated by average and standard deviations from 10 blanks. Detection limits were: 200 µg/L for Al, Fe, Mn, Mg, Na, K, Si and S; 500 µg/L for Ca; 50 µg/L for Zn; 5 µg/L for Cu; 2 µg/L for As and 1 µg/L for the other trace elements.

The X-ray diffraction (XRD) study of randomly oriented powder samples was performed using a Bruker D5005 X-ray Diffractometer with Cu Kα radiation at the CRSUH. Diffractometer settings were: 40 kV, 30 mA and a scan range of 2–65º 2θ, 0.05º 2θ step size and 20-s counting time per step.

Carbon-coated polished sections were studied with a JEOL JXA-8200 SuperProbe Electron Probe Micro-Analyzer (EPMA), using the fitted Wavelength-Dispersive Spectroscopy (WDS) equipment to obtain quantitative chemical analysis. The samples were analyzed for Al (Kα), Ca (Kα), Cu (Kα), Co (Kα), Fe (Kα), Ni (Kα), S (Kα), Si (Kα) and Zn (Kα). The following phases were used as standards: Al_2O_3 (Al), $CaSiO_3$ (Ca, Si), CuO (Cu), CoO (Co), Fe_2O_3 (Fe), NiO (Ni), $BaSO_4$ (S) and ZnO (Zn). Iron and aluminum precipitates were studied using an electron beam diameter of 10 µm while the smaller size of the zinc precipitates implied the use of a 1 µm electron beam. Detection limits for each element are presented in Table 2. Beam damage was minimal at operating conditions between 15 and 20 kV acceleration voltage and 10-20 nA intensity.

Powder solid samples were submitted to a 5 steps sequential extraction (SE) procedure, and the leachates analyzed as previously described for water samples. Step 1 is designed to obtain the water soluble fraction using deionizied water and shaking for 12 h at room temperature (RT). Step 2 employs 1 *M* NH_4-acetate buffer (pH 4.5) shaking for 1 h at RT to obtain the sorbed and exchangeable fraction and to completely dissolved calcite. Step 3 was employed to selectively dissolve poorly ordered Fe(III) oxyhydroxides and oxyhydroxisulfates by the use of 0.2 *M* NH_4-oxalate buffer (pH 3) shaking for 30 min in darkness and at RT. Step 4 apply the same reagent than Step 3 but using an 80 ºC water bath for 1 h to selectively dissolve the highly ordered Fe(III) hydroxides and oxides. Step 5 is a total digestion of the residue using HNO_3 + HF + $HClO_4$. A more detailed discussion of the selectivity in mineral dissolution and other properties of the reagents employed in the different SE steps can be found in Dold, 2003 and Caraballo et al., 2009b.

3. Results and discussion

3.1. Water chemistry temporal and spatial evolution within the reactive tank

First changes in the water chemistry take place within the supernatant body. As water from the adit contacts with atmosphere, Fe(II) is biologically oxidized to Fe(III), and the water reaches supersaturation with schwertmannite, precipitating this mineral along the conductions and within the supernatant water body. Precipitation of schwertmannite causes a concomitant decrease in pH and Fe from the supernatant (Figures 2 and 3). This pH decrement makes the water more aggressive and increase the efficiency of calcite dissolution.

AMD water chemistry and metal removal within the reactive tank are mainly controlled by the pH variations induced after limestone dissolution and to a less extent by the anaerobic and more reducing water environment developed at the bottom of the reactive mixture. The specific control exerted by limestone dissolution in the AMD hydrochemistry is shown in figure 2, where coupled to calcite dissolution (marked by a remarkable increment in water Ca concentration) a significant increase in water pH and alkalinity can be observed. Calcite dissolution, alkalinity generation and pH rise exhibit a close spatial and temporal evolution within the reactive material. As shown in figure 2, the sequence of calcite dissolution begins with a slight pH increase close to the reactive material surface and an almost imperceptible increment in water Ca concentration. As the water flows down the profile, water pH and Ca concentration gradually increase; however alkalinity generation only takes place after an important amount of calcite has been dissolved (Fig. 2). Water pH, Ca concentration and alkalinity remain constant from 65-80 cm depth (depending on the sampling campaign) to the bottom of the reactive material. The temporal sequence in Figure 2 shows a downward migration of the calcite dissolution front.

Fe and Al profiles show two distinctive redissolution and precipitation zones within the reactive material (Fig. 3). All those zones suffered a migration with time downward the reactive material profile, for this reason the beginning and end of those zones will be hereafter referred by a depth range. As shown in Figure 3, the first process taking place is a slight increment in Fe concentration and a decrease in pH (from 0 cm to 15-25 cm depth). These changes are similar to those observed in the aging experiments of schwertmannite to goethite (Acero et al, 2006). From 15-25 cm to 50-80 cm (Fe precipitation front) a progressive iron concentration decrease due to schwertmannite precipitation can be observed. The downward migration of the Fe precipitation zone forces the redissolution of the Al precipitates previously generated within the reactive material. This forced Al redissolution process is marked by the important increase in water Al concentration observed moving from 25 to 65 cm depth (Fig. 3). Subsequently to the cease of Fe removal, a complete Al removal takes place. The key factor for Al precipitation is the achievement of a pH higher than 5 (Bigham and Nordstrom, 2000; Caraballo et al., 2009b). This pH dependence is clearly observed in the sampling campaign corresponding to May 2008 where maximum Al concentration is obtained at 65 cm depth (Fig. 3) for a water pH of 4.8 (Fig. 2) while for the next sampling point at 80 cm depth the increase suffered by water pH (6.03) induce the total removal of Al from the water.

Chemically induced Zn, Co and Ni precipitation as hydroxides can only be expected after reaching a pH value higher than 8, 9 and 10 respectively (Cortina et al., 2003; Rötting et al., 2008a). However, the removal of these metals can also be induced by the generation of an anoxic and reducing water environment like the one present in wetlands or reactive barriers (Machemer et al., 1992; Benner et al., 1997; Ludwig et al, 2002, 2009). As can be observed in Figure 4, water redox environment evolves from very oxidizing at the water supernatant (Eh close to 700 mV) to reducing at the bottom of the reactive material (Eh values ranging from 154 to 277 mV). Coupled to this reducing environment generation, an important Zn, Ni and Co removal can be observed (Fig. 4). Zn removal pattern could be explained by two overlapping processes: (1) migration of a precipitation zone (from 177 to 230 cm depth) and (2) decrease with time of the removal capacity of the reducing environment. The first process can be observed in the sampling point at 177 cm depth where a significant removal was achieved in August 2007 while an important increase was measured in November 2007 and to a less extent in May 2008. The second process can be observed in the noticeable decrease with time of Zn in the sampling point at 230 cm depth (Fig. 4). Ni and Co removal is consistently confined to 230 cm depth, also showing an important decrease with time of the removal capacity. The increment in the output water concentration of the three metals is probably due to some redissolution of precipitates taking place at the limit between the reactive material and the quartz gravel drain. The presence of organic matter (wood shavings) in the reactive material and the two months that the reactive tank remained flooded previous to the system inauguration could have facilitated the growth of some sulfate reducing bacteria (SRB) within the reactive mixture, thus offering a possible explanation for the reducing environment observed. Migration of the

Al precipitation front confined Zn removal to the bottom part of the reactive material and could explain the decrease of Zn removal at the end of the experiment.

3.2 Mineralogical control on the reactive material performance and metal removal

All the information obtained for the mineralogical characterization of the different precipitates will be presented in three sub-sections corresponding to Fe, Al and Zn precipitation zones.

3.2.1 Iron precipitation zone

The Fe influence zone is restricted to the first 50 cm of the reactive material (Fig. 5). A first XRD approach to the mineralogy of the precipitates (Table 3) exposed the presence of schwertmannite as the only detected Fe mineral phase at 0-5 cm, followed by schwertmannite plus goethite at 5-15 cm and only goethite for the sample at 15-20 cm depth. There was not any detectable mineral phase in the samples at 20-35 and 35-50 cm depth (Table 3).

The results obtained after the sequential extraction performed to theses samples (Fig. 5) are in accordance with the XRD results. The presence of schwertmannite in the samples is marked by the Fe recovered at the third step of the sequential extraction while the Fe released at the fourth step is related to goethite dissolution. As can be observed, the Fe precipitation profile between 0 and 20 depth evolves from pure schwertmannite to a mixture of schwertmannite and goethite. This is consistent with the sedimentation on the water-reactive interface of the schwertmannite formed in the supernatant, followed of the ageing of the mineral to goethite, as previously reported in Fe-stromatolites (Acero et al., 2006; Asta et al., 2009) and passive treatment systems (Caraballo et al., 2009b; Gagliano et al., 2004). The sample at 20-35 cm depth corresponds to a level where no metal precipitation took place and only pine wood shavings were observed during the field sampling. Although the presence of any mineral phase was confirmed by XRD in the sample at 35-50 cm depth, the significant amount of Fe recovered in the third step of the sequential extraction can be attributed to the presence of schwertmannite. The recovery of an important concentration of S in Steps 2 and 3 is attributed to adsorbed and structural SO_4 in schwertmannite (Fig. 5). The absence of any recovered Ca at the second step of the sequential extraction confirms the complete calcite dissolution along the Fe precipitation zone and also corroborates the efficiency in limestone consumption before coating of the fine grains occurs.

To obtain a deeper characterization of schwertmannite (the main constituent of the Fe precipitation zone and mineral precursor of goethite) the composition and morphology of this mineral in sample 0-5 cm was investigated by EPMA. This study revealed the typical "sea urchin" morphology of schwertmannite forming associations of spheres ranging from 1 to 10 μm in diameter (Fig. 6A). Bulk chemistry for this mineral is offered in Table 2 where, as expected, Fe and S are the two main constituents. A small amount of Al, Ca and Si was also detected. On the basis of those analysis, the stoichiometry of the Mina Esperanza schwertmannite was deduced to be $Fe_8O_8(OH)_{4.56}(SO4)_{1.72}$:nH2O. The Fe/S molar ratio of 4.66 ± 0.07 obtained for schwertmannite in this study yield within the lower values of the broad range of 4.6-8.3 reported by several studies (Bigham and Nordstrom, 2000).

3.2.2 Aluminum precipitation zone

Aluminum precipitates are distributed from 50 to 180 cm depth exhibiting a decreasing tendency on the amount of precipitates downward the reactive material profile (Fig. 5). The XRD of the 6 samples from 50 to 180 cm depth (Table 3) only confirmed the presence of gypsum and calcite but no evidence of any Al mineral phases was observed. However the presence of basaluminite was confirmed by XRD on the particulate carried by the water at the output of the reactive tank. Al precipitates dissolution mainly took place at the third step of the sequential extraction where the extractant (0.2 *M* NH4-oxalate) is buffered at pH 3. A slight amount of Al is recovered at Step 2 (1 *M* NH4-acetate buffered at pH 4.5) and step 4 (0.2 *M* NH4-oxalate at pH 3 and 80 ºC) that could be attributed to an incipient Al precipitates dissolution at pH 4.5 and to the dissolution of a minor but more resistant Al-precipitate (Fig 5). Coupled to Al-precipitates dissolution a slight amount of S was recovered in Step 2 and 3 suggesting the presence of this element in the Al-precipitates. Al precipitates typically appear covering limestone grains and wood shavings (Fig. 6B). The chemical composition of those precipitates is offered in Table 2 where Al and S can be observed as the main constituents. The presence of minor amounts of other elements like Ca, Cu, Fe and Si was also consistently detected. The Al/S molar rates (from 3.37 to 4.96) observed at the four studied samples closely range the theoretical Al/S molar ratio of 4 calculated for basaluminite, $Al_4(SO_4)(OH)_{10}\cdot 5H_2O$, or its precursor hydrobasaluminite, $Al_4(SO_4)(OH)_{10}\cdot 12\text{-}36H_2O$. These Al/S ratios observed and the detection of basaluminite by XRD as the only Al mineral phase at the output of the reactive tank, confirm this mineral and its precursor hydrobasaluminite as the main Al mineral phase controlling Al precipitation within the reactive tank, although the presence of minor amounts of other poorly crystalline or amorphous Al-precipitates can not be completely rule out.

Gypsum precipitation can be observed (from equimolal Ca and S released in Step 1, Fig. 5) coupled to the Al precipitation zone but showing an inverse tendency (increasing with depth). Ca release in the second step of the sequential extraction can be attributed to the selective dissolution of calcite and, as shown in Figure 5, the presence of this mineral is observed along the Al precipitation zone. The presence of calcite and gypsum was also confirmed by XRD in all the samples from 50 to 220 cm depth (Table 3).

The sample at 180-215 cm depth corresponds to a section of un-reacted material mainly composed by limestone and wood shavings, and shows a small amount of gypsum as the only neoformed mineral phase (Fig. 5 and Table 3).

3.2.3 Zinc precipitation zone

Divalent metals like Zn, Ni and Co were found to be selectively precipitated in the deeper section of the reactive material profile (Fig. 7). Those three metals are predominantly recovered in the second step of the sequential extraction and display their maximum concentrations in the sample at 240-250 cm depth that is in accordance with the important Zn, Ni and Co removal from the pore water observed for the sampling tube at 230 cm depth (Fig. 4). The specific recovery of those elements in the second step of the sequential extraction rule out the possibility of any kind of sulfur as hosting mineral because this step is designed to dissolved calcite or at least more labile mineral phases. The morphological and chemical study performed with EPMA showed those three elements hosted in aggregates of micro spheres of 1-2 μm in diameter (Fig. 6), exhibiting a great resemblance with the spherical morphology observed for schwertmannite in the Fe precipitation zone. On the basis of the chemical analysis performed to this sample (Table 2), Fe, Zn and S were detected as the main constituents of the precipitates. Al, Ca and Si were detected on a significant but much smaller proportion and finally Cu, Co and Ni as minor constituents.

Previous studies have described the appearance of Fe(II)-Fe(III) “green rust” minerals in reductomorphic soils (Bourrié et al., 1999; Feder et al., 2005; Trolard, 2006) . Those soils are characterized by an excess of water, the restriction of the oxygen sources, the presence of bio-available substrates and the presence of elements able to change their oxidation state (Trolard, 2006), being all these characteristic present in the deeper part of the reactive tank in Mina Esperanza. “Green rust” compounds have the normalized chemical formula $[\mathrm{Fe}^{\mathrm{II}}_{1-x}\mathrm{Fe}^{\mathrm{III}}_{x}(\mathrm{OH})_2]^{x+}$ $[(x/n)\mathrm{A}^{n-}\cdot(mx/n)\mathrm{H_2O}]^{x-}$, where positively charged hydroxide layers $[\mathrm{Fe}^{\mathrm{II}}_{1-x}\mathrm{Fe}^{\mathrm{III}}_{x}(\mathrm{OH})_2]^{x+}$ alternate with negatively charged interlayers of anions A^{n-} ($\mathrm{CO_3}^{2-}$, $\mathrm{SO_4}^{2-}$, Cl^{-}, …) and with m water molecules per anion. Cations substitutions have also been observed and Fe^{2+} substitution by Zn^{2+} has been specifically reported for synthetic samples (Zhang et al., 2007). The presence of “green rust” minerals in low redox AMD environments has also been proposed from the thermodynamically point of view (Majzlan et al., 2004) and directly observed in passive treatments using zerovalent iron (Bartzas and Komnitsas, 2010; Lien and Wilkin, 2005).

On the basis of the hydrochemical environment and the chemical composition of the precipitates, a poorly crystalline sulfate “green rust” with a significant substitution of Zn is proposed as the most plausible mineral phase responsible of Zn, Ni and Co removal at the bottom section of the reactive tank.

3.3. Reactive material hydraulic conductivity, performance evolution and future design considerations.

Clogging problems by neoformed minerals in the pore space of the reactive material and the subsequent loss of hydraulic conductivity leading to the failure of the treatment operation is one of the most common difficulties that a passive treatment design must overcome. The design implemented in Mina Esperanza uses a high-porosity reactive material with 1 m of free wall in the reactive tank (Fig. 1) to compensate the increase in the supernatant water level as a result of the induced metal precipitation in the pore space of the reactive material. The effectiveness of this design was reflected in the steady high flow, ranging from 43 to 86 m^3/day, observed during the 20 months of operation time.

To gain a better understanding of the reactive material performance against the expected clogging problems, the hydraulic conductivity time evolution was calculated (Eq. 1). The results distinctly fit an exponential decay regression line for the first year of operation, moving from an initial hydraulic conductivity of approximately 6 m/day to a final value close to 1 m/day (Fig. 8). But subsequently, the hydraulic conductivity steady range 1 m/day for the last 8 months of operation. Although the evolution of the hydraulic conductivity of a DAS reactive material submitted to a longer operation time can only be certainly known after the study of a new longer field experiment, the tendency showed by this parameter during 20 months of operation suggests the achievement of a longer operation time as an encouraging possibility.

As shown in this study, there was an important amount of undissolved calcite from 85 to 250 cm depth (Fig. 5). However, the low pH (5.14) and alkalinity (35 mg/L as $CaCO_3$ equivalents) observed at the output of the reactive tank during the last sampling campaign (October 2008) imply a substantial decrease in the reactivity of the substrate. On the light of the hydrobasaluminite distribution showed in this study, calcite partial passivation by surface armoring (Fig.6) is proposed, in addition to calcite consumption, as the main process responsible of the substrate reactivity loss.

Despite the high performance achieved by the reactive tank in Mina Esperanza 2007-2008, some improvements in the original design are planned to be incorporated in the future treatment to be implemented in 2011. On the basis of the hydraulic conductivity evolution observed and to achieve a cost-efficient use of the reactive material, we suggest establishing an operating period of two years for the reactive material. To extend the reactivity of the reactive material, we also suggest increasing the amount of limestone employed. Another possibility that is being taking into account is the inclusion of new reagents to the limestone-DAS at the deeper section of the reactive material in order to enhance the reducing environment and to promote divalent metals removal. The addition to some zerovalent iron is being considered as an option to promote the desired reducing environment. A second option would be the inclusion of organic matter to the last 0.5 m of the limestone-DAS reactive material. This organic matter could promote sulfate reducing bacteria activity and subsequently maintain the reducing environment. A mixture of these two materials has been recently found efficient in metal removal (Ludwig et al., 2009), and are currently under study by means of laboratory experiments.

Acknowledgments

We gratefully acknowledge Mari Paz Martín, Rafael Carrasco and María José Ruíz, and Cristobal Cantero (Central Research Services of the University of Huelva) for assistance in XRD, ICP-OES and EPMA, respectively. This study was funded by the Spanish Ministry of Science and Technology through the projects CTM2007-66724-C02/TECNO and CTM2010-21956-C02 and by the Environmental Council of the Andalusia Regional Government. M.A.C. was financially supported by the Spanish Government with a FPU PhD fellowship.

References

Acero, P., Ayora, C., Torrentó, C., and Nieto, J.-M. (2006) The behavior of trace elements during schwertmannite precipitation and subsequent transformation into goethite and jarosite. Geochimica et Cosmochimica Acta, 70(16), 4130-4139.

Asta, M.P., Ayora, C., Román-Ross, G., Cama, J., Acero, P., Gault, A.G., Charnock, J.M., and Bardelli, F. (2009) Natural attenuation of arsenic in the Tinto Santa Rosa acid stream (Iberian Pyritic Belt, SW Spain): The role of iron precipitates. Chemical Geology, 271(1-2), 1-12.

Bartzas, G., and Komnitsas, K. (2010) Solid phase studies and geochemical modelling of low-cost permeable reactive barriers. Journal of Hazardous Materials, 183(1-3), 301-308.

Benner, S. G., Blowes, D. W., Ptacek, C. J. (1997) A full-scale porous reactive wall for prevention of acid mine drainage. Ground Water Monitoring and Remediation, 17, 99-107.

Bigham, J.M., and Nordstrom, D.K. (2000) Iron and Aluminum Hydroxysulfates from Acid Sulfate Waters. In C.N. Alpers, J.L. Jambor, and D.K. Nordstrom, Eds. Sulfate Minerals: Crystallography, Geochemistry, and Environmental Significance, 40, p. 351-403. Reviews in Mineralogy and Geochemistry, Mineralogical Society of America., Chantilly, Virginia.

Bourrié, G., Trolard, F., Jaffrezic, J.-M.R.G., MaItre, V., and Abdelmoula, M. (1999) Iron control by equilibria between hydroxy-Green Rusts and solutions in hydromorphic soils. Geochimica et Cosmochimica Acta, 63(19-20), 3417-3427.

Caraballo, M.A., Rötting, T.S., Macías, F., Nieto, J.M., and Ayora, C. (2009a) Field multi-step limestone and MgO passive system to treat acid mine drainage with high metal concentrations. Applied Geochemistry, 24(12), 2301-2311.

Caraballo, M.A., Rotting, T.S., Nieto, J.M., and Ayora, C. (2009b) Sequential extraction and DXRD applicability to poorly crystalline Fe- and Al-phase characterization from an acid mine water passive remediation system. American Mineralogist, 94(7), 1029-1038.

Caraballo, M.A., Santofimia, E., and Jarvis, A.P. (2010) Metal retention, mineralogy, and design considerations of a mature permeable reactive barrier (PRB) for acidic mine water drainage in Northumberland, U.K. American Mineralogist, 95(11-12), 1642-1649.

Cortina, J.L., Lagreca, I., De Pablo, J., Cama, J., and Ayora, C. (2003) Passive In Situ Remediation of Metal-Polluted Water with Caustic Magnesia: Evidence from Column Experiments. Environ. Sci. Technol., 37(9), 1971-1977.

Dold, B. (2003) Speciation of the most soluble phases in a sequential extraction procedure adapted for geochemical studies of copper sulfide mine waste. Journal of Geochemical Exploration, 80(1), 55-68.

Feder, F., Trolard, F., Klingelhöfer, G., and Bourrié, G. (2005) In situ Mössbauer spectroscopy: Evidence for green rust (fougerite) in a gleysol and its mineralogical transformations with time and depth. Geochimica et Cosmochimica Acta, 69(18), 4463-4483.

Gagliano, W.B., Brill, M.R., Bigham, J.M., Jones, F.S., and Traina, S.J. (2004) Chemistry and mineralogy of ochreous sediments in a constructed mine drainage wetland. Geochimica et Cosmochimica Acta, 68(9), 2119-2128.

Jarvis, A.P., Moustafa, M., Orme, P.H.A., and Younger, P.L. (2006) Effective remediation of grossly polluted acidic, and metal-rich, spoil heap drainage using a novel, low-cost, permeable reactive barrier in Northumberland, UK. Environmental Pollution, 143(2), 261-268.

Johnson, D.B., and Hallberg, K.B. (2005) Acid mine drainage remediation options: a review. Science of The Total Environment, 338(1-2), 3-14.

Lien, H.-L., and Wilkin, R.T. (2005) High-level arsenite removal from groundwater by zero-valent iron. Chemosphere, 59(3), 377-386.

Ludwig, R. D., McGregor, R. G., Blowes, D. W., Benner, S. G., Mountjoy, K. (2002) A permeable reactive barrier for treatment of heavy metals. Ground Water, 40 (1), 59-66

Ludwig R.D., Smyth D.J.A., Blowes D.W., Spink L.E., Wilkin R.T., Jewett D.G., Weisener C.J. (2009) Treatment of Arsenic, Heavy Metals, and Acidity Using a Mixed ZVI-Compost PRB. Environmental Science & Technology, 43 (6): 1970-1976

Machemer, S. D., Wildemann, T. R. (1992) Adsorption compared with sulphide precipitation as a metal removal processes from acid mine drainage in a constructed wetland. Journal of Contaminant Hydrology, 9, 115-131

Majzlan, J., Navrotsky, A., and Schwertmann, U. (2004) Thermodynamics of iron oxides: Part III. Enthalpies of formation and stability of ferrihydrite (~Fe(OH)3), schwertmannite (~FeO(OH)3/4(SO4)1/8), and [var epsilon]-Fe2O3. Geochimica et Cosmochimica Acta, 68(5), 1049-1059.

Nocete, F., Álex, E., Nieto, J.M., Sáez, R., and Bayona, M.R. (2005) An archaeological approach to regional environmental pollution in the south-western Iberian Peninsula related to Third millennium BC mining and metallurgy. Journal of Archaeological Science, 32(10), 1566-1576.

Rötting, T.S., Ayora, C., and Carrera, J. (2008a) Improved Passive Treatment of High Zn and Mn Concentrations Using Caustic Magnesia (MgO): Particle Size Effects. Environmental Science & Technology, 42(24), 9370-9377.

Rötting, T.S., Caraballo, M.A., Serrano, J.A., Ayora, C., and Carrera, J. (2008b) Field application of calcite Dispersed Alkaline Substrate (calcite-DAS) for passive treatment of acid mine drainage with high Al and metal concentrations. Applied Geochemistry, 23(6), 1660-1674.

Rötting, T.S., Thomas, R.C., Ayora, C., and Carrera, J. (2008c) Passive Treatment of Acid Mine Drainage with High Metal Concentrations Using Dispersed Alkaline Substrate. J Environ Qual, 37(5), 1741-1751.

Sáez, R., Pascual, E., Toscano, M., and Almodóvar, G.R. (1999) The Iberian type of volcano-sedimentary massive sulphide deposits. Mineralium Deposita, 34(5), 549-570.

Sarmiento, A.M., Nieto, J.M., Olías, M., and Cánovas, C.R. (2009) Hydrochemical characteristics and seasonal influence on the pollution by acid mine drainage in the Odiel river Basin (SW Spain). Applied Geochemistry, 24(4), 697-714.

Tyler, G., Carrasco, R., Nieto, J.M., Perez, R., Ruiz, M.J., Sarmiento, A.M., 2004. Optimization of Mayor and Trace Element Determination on Acid Mine Drainage samples by Ultrasonic Nebulizer-ICP-OES (USN-ICP-OES) Pittcon Conf. 7–12 March. Chicago, USA.

Trolard, F. (2006) Fougerite: From field experiment to the homologation of the mineral. Comptes Rendus Geosciences, 338(16), 1158-1166.

Younger, P.L., Banwart, S.A., and Hedin, R.S. (2002) Mine Water: Hydrology, Pollution, Remediation. Kluwer Academic Publishers, Dordrecht.

Zhang, H., Wen, X., and Wang, Y. (2007) Synthesis and characterization of sulfate and dodecylbenzenesulfonate intercalated zinc-iron layered double hydroxides by one-step coprecipitation route. Journal of Solid State Chemistry, 180(5), 1636-1647.

FIGURE CAPTIONS

FIGURE 1A). Location of the passive treatment system in Mina Esperanza B) Cross section of the reactive tank in Mina Esperanza.

FIGURE 2. Chemical profiles of pore water showing Ca, Alkalinity and pH vertical distribution and evolution within the reactive tank. 0 cm depth corresponds to the surface of the reactive material.

FIGURE 3. Vertical distribution and temporal evolution of Fe and Al concentrations in the pore waters flowing through the reactive tank. 0 cm depth corresponds to the surface of the reactive material. Arrows mark the migration of the Fe and Al redissolution and precipitation fronts.

FIGURE 4. Chemical profile showing Eh, Zn, Ni and Co vertical distribution and temporal evolution in pore water within the reactive tank. 0 cm depth corresponds to the surface of the reactive material.

FIGURE 5. Cumulative graphs for the concentration of the main constituent (Fe, Al, Ca and S) elements obtained after each step of the sequential extraction for the different solid samples studied.

FIGURE 6. EPMA images of the precipitates in the different reactive zones; from top to bottom: A) Iron zone; B) Aluminum zone; C) Zinc zone.

FIGURE 7. Cumulative graphs for the concentration of Zn, Ni and Co obtained after each step of the sequential extraction for the different solid samples studied.

FIGURE 8. Evolution of the hydraulic conductivity in the reactive material.

TABLES

TABLE 1. AMD composition and physical-chemical parameters at the adit.

TABLE 2. Representative EMPA analysis of six selected samples within the reactive tank. Presented values (wt %) correspond to mean value and Detection limits are presented below each element label.

TABLE 3. Mineral phases confirmed by XRD.

Fig. 1

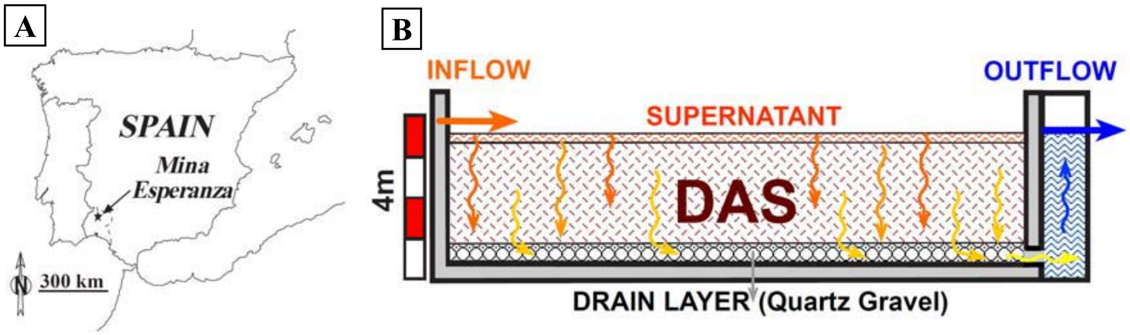
A
SPAIN
Mina
Esperanza
N
300 km
B
INFLOW
OUTFLOW
SUPERNATANT
4m
DAS
DRAIN LAYER (Quartz Gravel)

Fig. 2

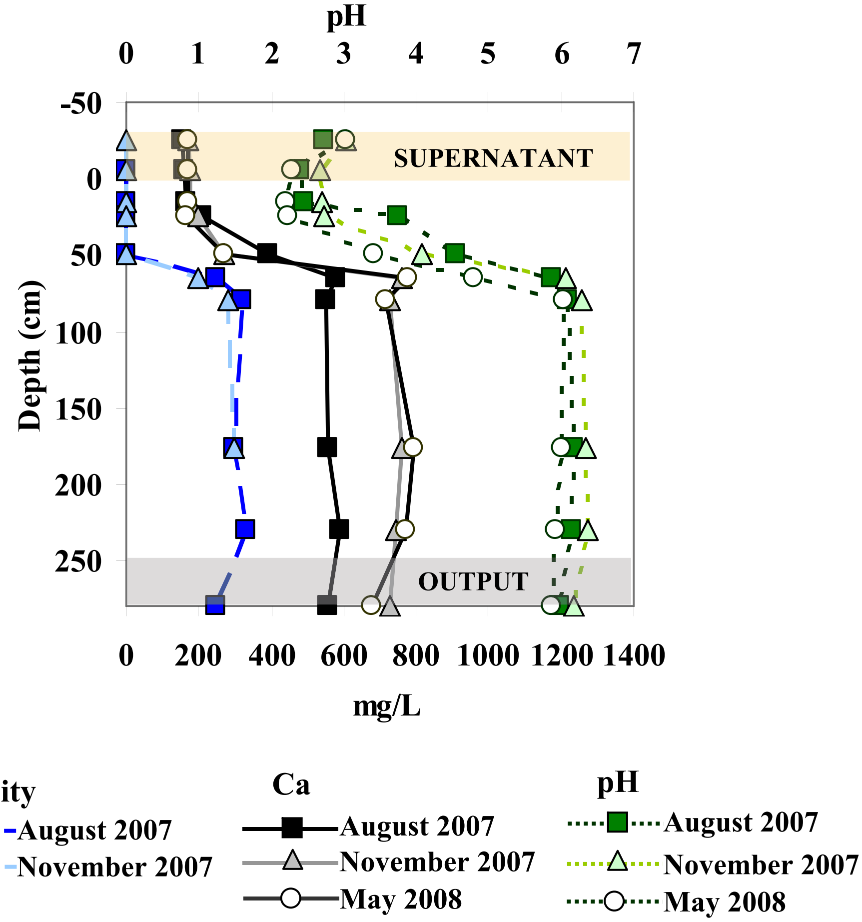

pH
0
1
2
3
4
5
6
7
-50
0
50
100
150
200
250
Depth (cm)
SUPERNATANT
OUTPUT
0
200
400
600
800
1000
1200
1400
mg/L
Alkalinity
August 2007
November 2007
Ca
August 2007
November 2007
May 2008
pH
August 2007
November 2007
May 2008

Fig. 3

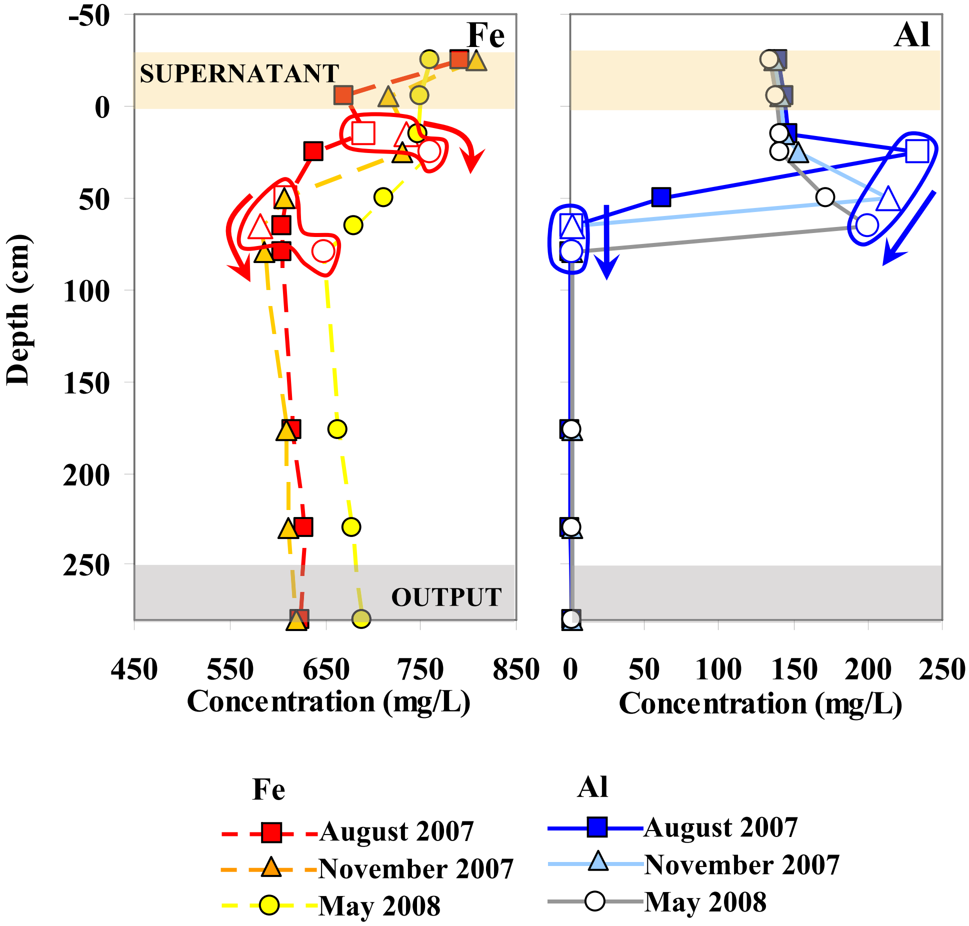
Fe
SUPERNATANT
OUTPUT
Al
-50
0
50
100
150
200
250
Depth (cm)
450
550
650
750
850
Concentration (mg/L)
0
50
100
150
200
250
Concentration (mg/L)
Fe
August 2007
November 2007
May 2008
Al
August 2007
November 2007
May 2008

Fig. 4

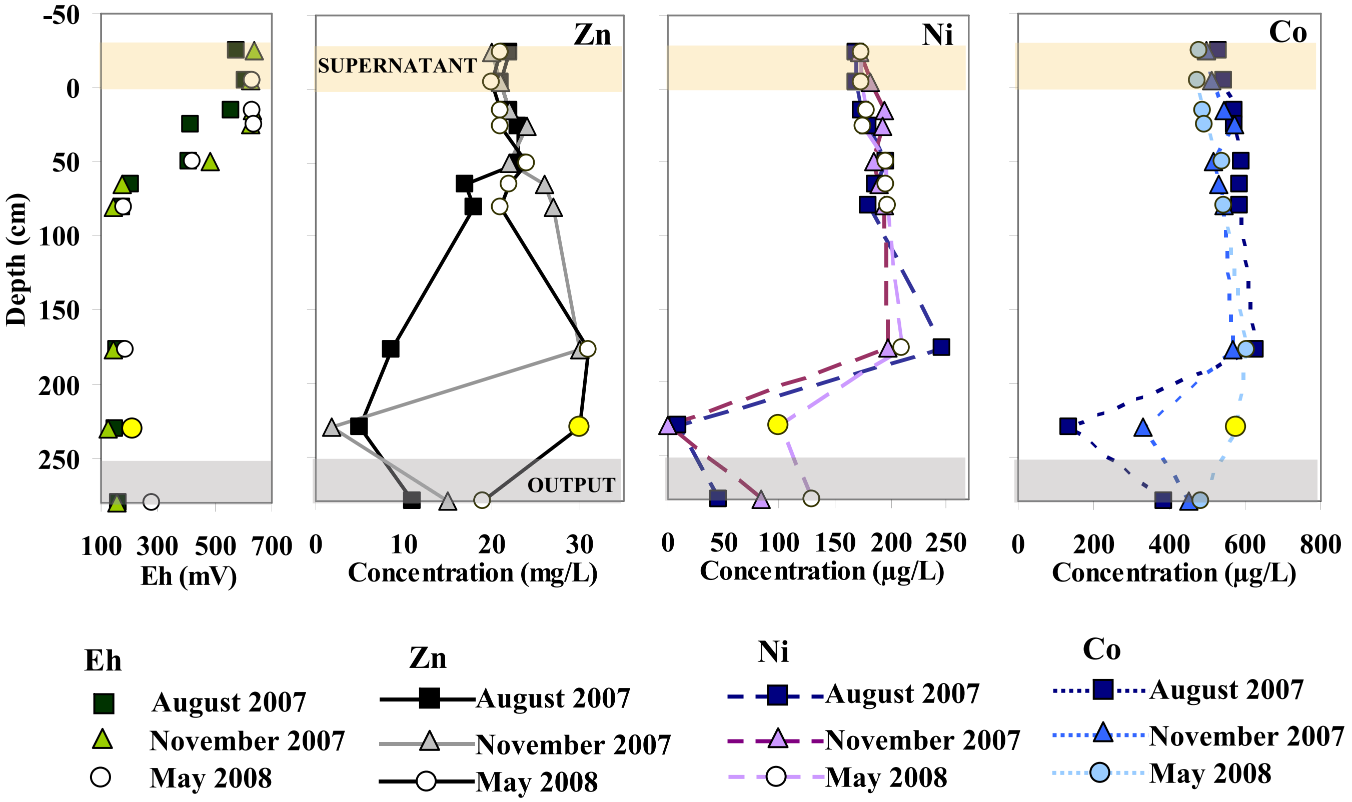
Depth (cm)
-50
0
50
100
150
200
250
100 300 500 700
Eh (mV)
Zn
SUPERNATANT
OUTPUT
0 10 20 30
Concentration (mg/L)
Ni
0 50 100 150 200 250
Concentration (µg/L)
Co
0 200 400 600 800
Concentration (µg/L)
Eh
August 2007
November 2007
May 2008
Zn
August 2007
November 2007
May 2008
Ni
August 2007
November 2007
May 2008
Co
August 2007
November 2007
May 2008

Fig. 5

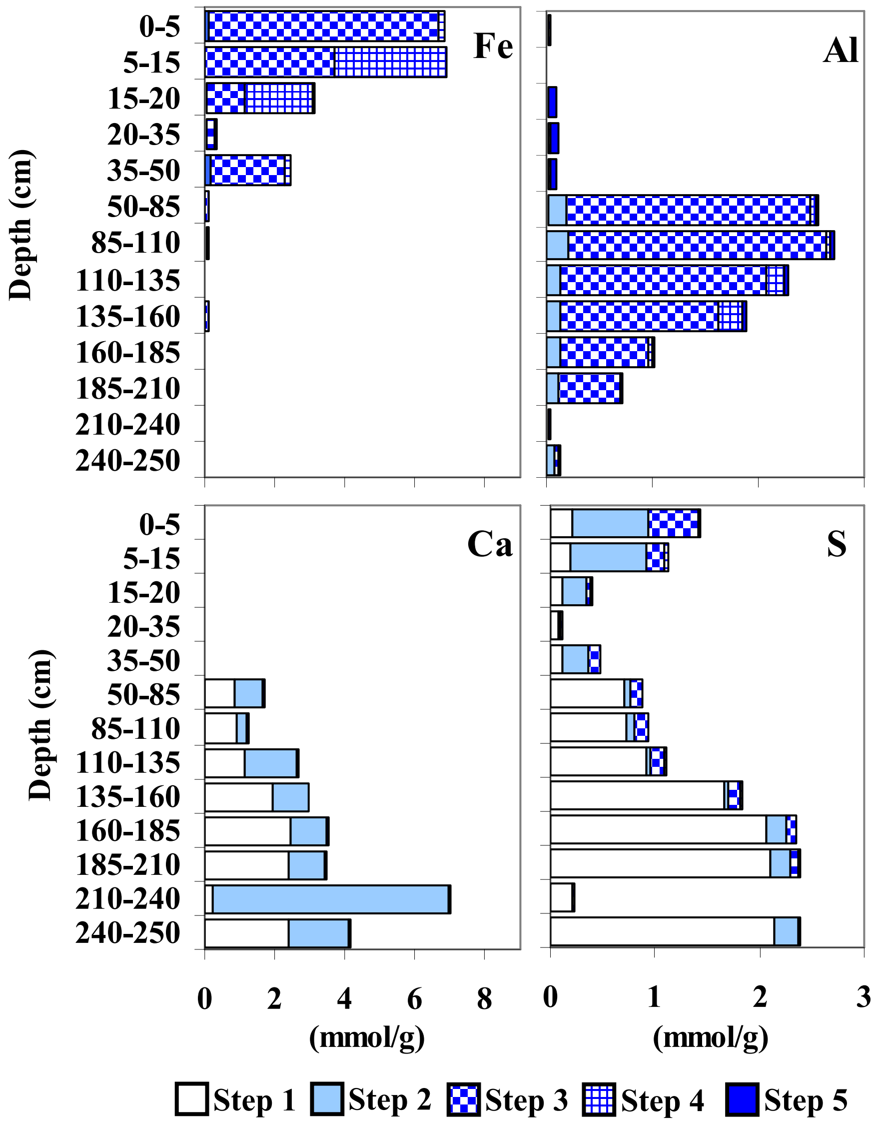

Fe
Al
Ca
S
Depth (cm)
0-5
5-15
15-20
20-35
35-50
50-85
85-110
110-135
135-160
160-185
185-210
210-240
240-250
0
2
4
6
8
0
1
2
3
(mmol/g)
(mmol/g)
Step 1
Step 2
Step 3
Step 4
Step 5

Fig. 6

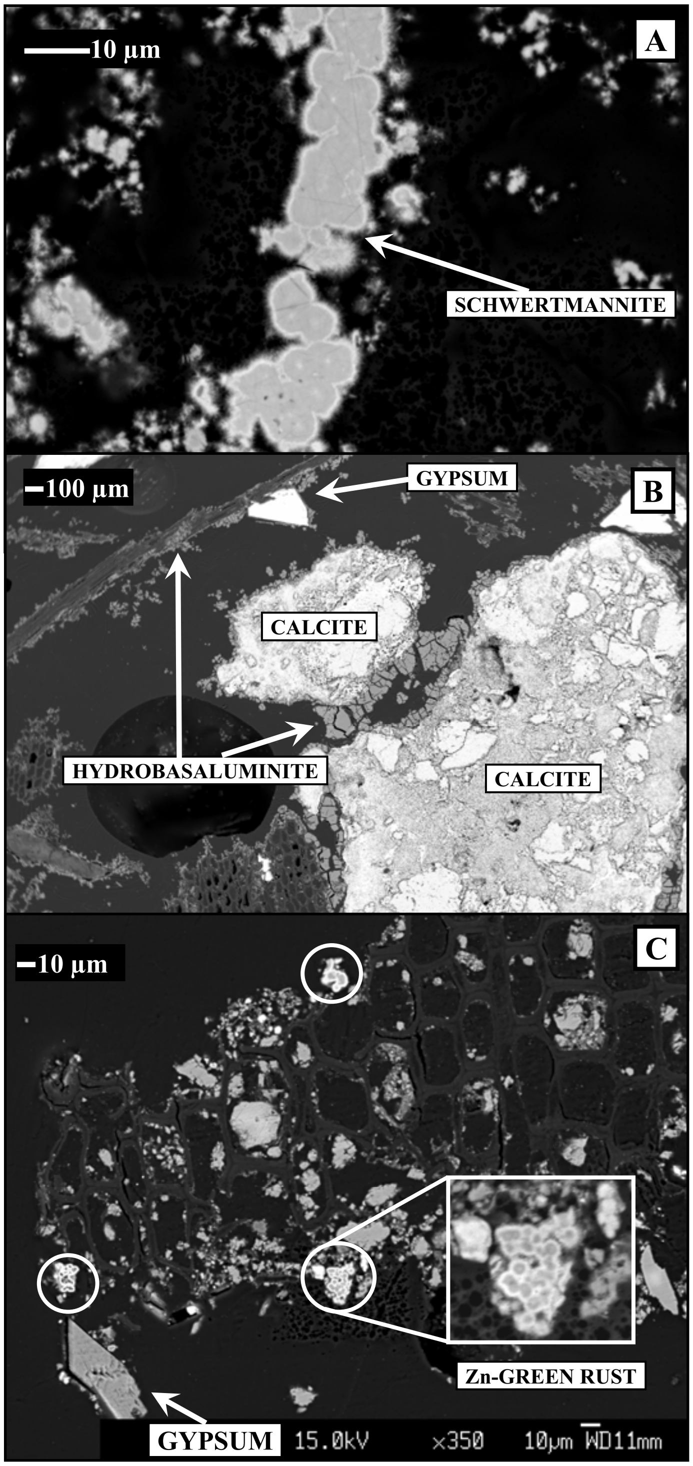
10 µm
A
SCHWERTMANNITE
100 µm
GYPSUM
B
CALCITE
HYDROBASALUMINITE
CALCITE
10 µm
C
Zn-GREEN RUST
GYPSUM
15.0kV ×350 10µm WD11mm

Fig. 7

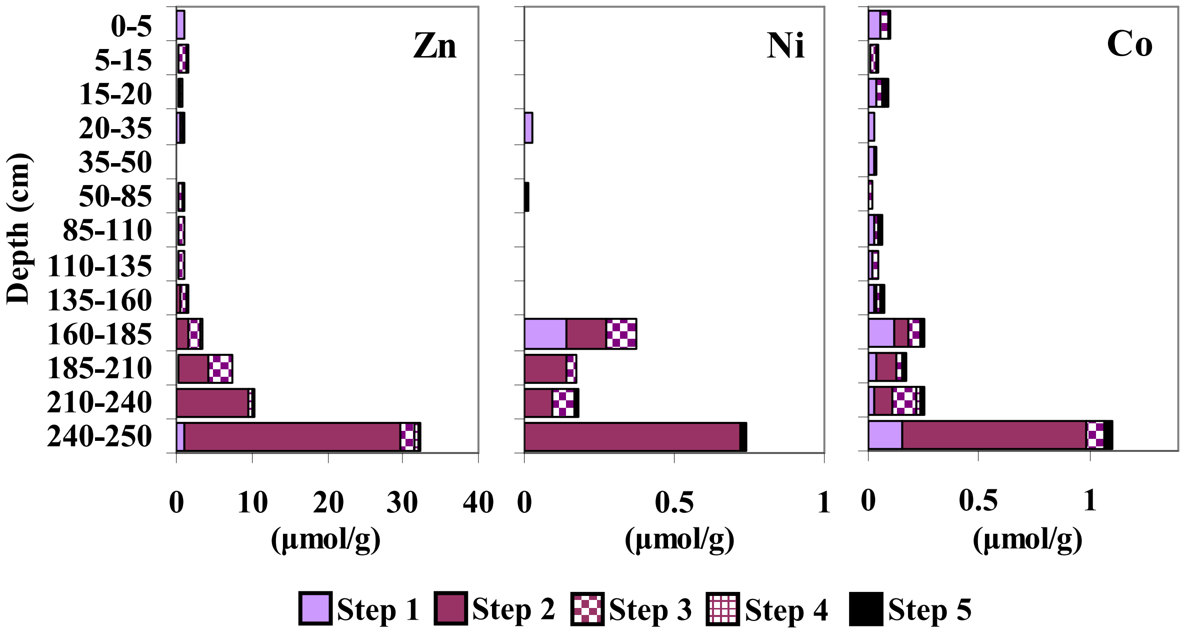

Depth (cm)
0-5
5-15
15-20
20-35
35-50
50-85
85-110
110-135
135-160
160-185
185-210
210-240
240-250
Zn
Ni
Co
0
10
20
30
40
0
0.5
1
0
0.5
1
(µmol/g)
(µmol/g)
(µmol/g)
Step 1
Step 2
Step 3
Step 4
Step 5

Fig. 8

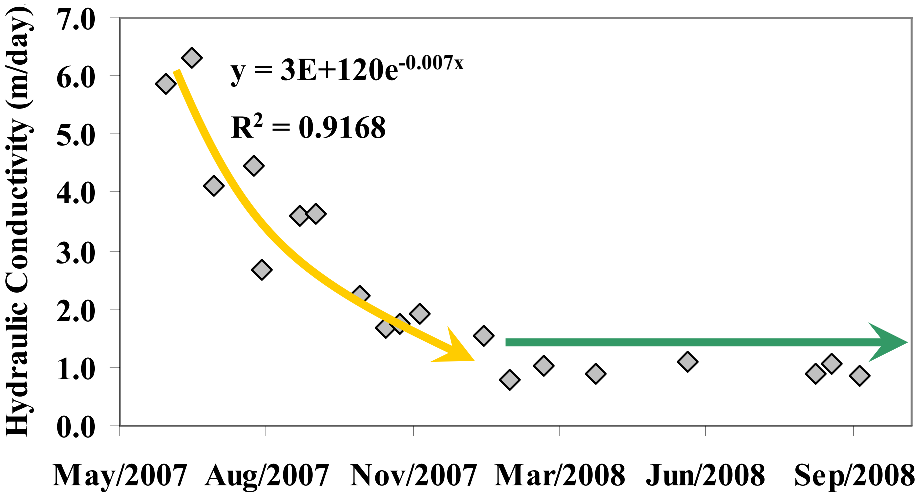

Hydraulic Conductivity (m/day)
7.0
6.0
5.0
4.0
3.0
2.0
1.0
0.0
y = 3E+120e-0.007x
R2 = 0.9168
May/2007
Aug/2007
Nov/2007
Mar/2008
Jun/2008
Sep/2008

Table1. AMD composition and physical-chemical parameters at the adit

Major elements (mg/L

Al	Ca	Cu	Fe	K	Mg	Mn	Na	SO_4^{2-}	Si	Zn
128-167	146-194	12-24	755-1100	5-34	149-215	4-6	21-26	3324-4515	44-60	19-33

Minor elements (µg/L

As	Ba	Be	Cd	Co	Cr	Li	Ni	Sr	Ti	V
357-692	4-6.5	4-10	66-98	468-759	22-42	138-381	152-247	131-189	6.5-15	84-129

Physical-chemical parameters

pH	Eh	Conductivity (mS/cm)	T (ºC)	Dissolved Oxygen (mg/L)	Dissolved oxygen (%)
2.35-2.96	555-597	3.24-6.12	16.8-22.2	1.8-2.5	13-28

Minimun and maximun values obtained in the 42 samplings campaign (March 2007-October 2008)

Table 2. Representative EMPA analysis of six selected samples within the reactive tank. Presented values (wt %) correspond to mean value and standar deviation of 30 analysis obtained in each sample.

Depth (cm)	Al_2O_3	CaO	CuO	CoO	FeO	SO_3	SiO_2	NiO	ZnO	Fe/S $_{\text{molar}}$	Al/S $_{\text{molar}}$
	(0.02)	(0.02)	(0.05)	(0.08)	(0.05)	(0.03)	(0.03)	(0.08)	(0.08)		
0-5	0.12 ± 0.03	0.09 ± 0.07	n.d.	n.d.	56.70 ± 1.18	13.58 ± 0.17	0.30 ± 0.07	n.d.	n.d.	4.66 ± 0.07	-
85-110	40.10 ± 1.24	0.13 ± 0.05	0.85 ± 0.33	n.d.	0.15 ± 0.05	18.69 ± 0.77	2.10 ± 0.41	n.d.	b.d	-	3.37 ± 0.16
135-160	43.15 ± 1.48	0.93 ± 0.60	1.89 ± 1.30	n.d.	0.33 ± 0.12	13.99 ± 2.18	1.33 ± 0.21	n.d.	0.17 ± 0.14	-	4.96 ± 0.82
160-185	57.82 ± 3.81	0.04 ± 0.02	0.97 ± 0.31	n.d.	0.34 ± 0.07	20.65 ± 0.45	0.80 ± 0.28	n.d.	b.d.	-	4.40 ± 0.27
185-210	46.48 ± 3.01	0.67 ± 0.51	0.53 ± 0.41	n.d.	0.15 ± 0.07	16.02 ± 1.77	0.91 ± 0.14	n.d.	0.50 ± 0.39	-	4.62 ± 0.69
240-250	3.89 ± 2.54	1.83 ± 0.54	0.22 ± 0.14	0.37 ± 0.11	48.37 ± 3.72	9.52 ± 2.13	1.68 ± 0.31	0.37 ± 0.20	12.08 ± 2.58	-	-

Detection limits are presented below each element label. b.d. = below detection limit, n.d. = not detected

Table 3. Mineral phases confirmed by XRD

Depth (cm)	Schwertmannite	Goethite	Gypsum	Calcite
0-5	X	-	-	-
5-15	X	X	-	-
15-20	-	X	-	-
20-35	-	-	-	-
35-50	-	-	-	-
50-85	-	-	X	X
85-110	-	-	X	X
110-130	-	-	X	X
130-150	-	-	X	X
150-165	-	-	X	X
165-180	-	-	X	X
180-215	-	-	X	X
215-220	-	-	X	X